

See discussions, stats, and author profiles for this publication at: <https://www.researchgate.net/publication/335426648>

Inverse design of structural color using machine learning

Article in *Nanoscale* · August 2019

DOI: 10.1039/C9NR06127D

CITATIONS

0

READS

126

3 authors, including:



Jianfeng Zang

Huazhong University of Science and Technology

79 PUBLICATIONS 2,835 CITATIONS

[SEE PROFILE](#)



Zhao Huang

Huazhong University of Science and Technology

6 PUBLICATIONS 144 CITATIONS

[SEE PROFILE](#)

Some of the authors of this publication are also working on these related projects:



Stretchable electronics [View project](#)



Thermal Transport in Soft PAAm Hydrogels [View project](#)



Cite this: DOI: 10.1039/c9nr06127d

The inverse design of structural color using machine learning†

Zhao Huang,^{a,b} Xin Liu^{a,b} and Jianfeng Zang  *^{a,b}

Efficiently identifying optical structures with desired functionalities, referred to as inverse design, can dramatically accelerate the invention of new photonic devices, and this is especially useful in the design of large scale integrated photonic chips. Structural color with high-resolution, high-saturation, and low-loss holds great promise in image display, data storage and information security. However, the inverse design of structural color remains an open challenge, and this impedes practical application. Here, we propose an inverse design strategy for structural color using machine learning (ML) technologies. The supervised learning (SL) models are trained with the geometries and colors of dielectric arrays to capture accurate geometry-color relationships, and these are then applied to a reinforcement learning (RL) algorithm in order to find the optical structural geometries for the desired color. Our work succeeds in finding simple and accurate models to describe geometry-color relationships, which significantly improves the efficiency of the design. This strategy provides a systematic method to directly encode generic functionality into a set of structures and geometries, paving the way for the inverse design of functional photonic devices.

Received 19th July 2019,
Accepted 25th August 2019
DOI: 10.1039/c9nr06127d
rsc.li/nanoscale

1. Introduction

Photonic devices with new functionalities have emerged with the development of new materials, fabrication processes, and optical structures.^{1–5} The design of photonic devices is usually based on intuition through trial-and-error methods.⁶ The design procedure can be summarized in two key steps: (1) Materials and optical structures are determined based on known physical effects. (2) The specific functionalities of the photonic devices are achieved by trying various factors including compositions and geometry parameters. Many efforts have been made to improve the efficiency of the design through optimization approaches such as using a genetic algorithm, a gradient descent method and topology optimization.^{7,8} These optimization methods have stimulated the development of nonlinear, topological, and near-field optics. However, conventional design and optimization methods remain significant challenges with the increasing complexity of the on-demand functionalities and integration level of optical devices.

Fortunately, advances in artificial intelligence (AI) technology have prompted a settlement of this dilemma. Machine learning (ML) is a statistics technology that trains a machine by telling it what to do. ML plays crucial roles in computer vision, natural language processing, robot control, and other AI applications.^{9,10} The capability of dealing with complex behaviors and big data makes ML a prominent technique in science and engineering.^{11–17} In materials science, ML has succeeded in guiding the chemical synthesis and discovery of suitable compounds with target properties.^{18–21} In biogenetics, analyzing large genomic data through ML has helped to annotate various genomic elements, and this is useful in gene recognition and editing.^{22,23} Moreover, significant progress has been made in photonics using ML technology, such as in the pattern recognition of photonic modes, the analysis of modulation instability in optical fibers and in the rational structure design for waveguides.^{24–29} Most recently, neural networks in a tandem architecture have been proposed to solve the inverse design problems of nanophotonic structures, which provides an opportunity to revolutionize the optical device design. Dianjing Liu *et al.* proposed a tandem architecture composed of an inverse design network connected to a forward modeling network, and this allowed the deep neural networks to effectively solve the non-unique inverse design problem. Such structures have been applied to the inverse design of topological photonics, core-shell nanoparticles and plasmonic waveguides.^{30–33} Deep learning networks have made great success in solving the inverse design problems. However, such

^aSchool of Optical and Electronic Information and Wuhan National Laboratory for Optoelectronics, Huazhong University of Science and Technology, Wuhan, China, 430074. E-mail: jjzhang@hust.edu.cn

^bInnovation Institute, Huazhong University of Science and Technology, Wuhan, China, 430074

† Electronic supplementary information (ESI) available. See DOI: 10.1039/c9nr06127d

a strategy requires large amounts of data, which makes it less efficient compared with simple models when dealing with a system that consists of few features.

Structural color holds great promise in display and security technology.^{34–41} Devices that consist of metallic or dielectric nanostructures can provide high resolution, and low-loss full color displays.^{42–46} However, the existing design approach is inefficient due to the complexity of the geometry-color relationship, which prevents structural color from reaching scalable fabrication. It is crucial to achieve a new structural color design strategy through the direct identification of structure geometries for each desired color property. Here, we propose an inverse design strategy for structural color using supervised learning (SL) and reinforcement learning (RL). We train the SL models to capture the geometry-color relationships in structural color and introduce a RL algorithm together with the SL models to efficiently identify the structure geometries that generate the desired colors. We demonstrate our strategy by designing both ring and pyramid resonator arrays. Our strategy achieves inverse design with high reliability and accuracy and can be applicable to the design of a wide range of functional materials.

2. Results and discussion

2.1. Inverse design framework

Our inverse design strategy for structural color is schematically illustrated in Fig. 1, and consists of three key steps: establishing the datasets, training the SL models, and implementing the RL algorithms. The datasets are made up of two parts: structure geometries and color properties. The color properties

of the given geometries are obtained from the FEM simulation. During the training process, correlation analysis and optimization techniques such as grid searching and cross-validation were applied to improve the performance of the SL models. Finally, the RL algorithm was implemented with the help of the trained SL models to efficiently identify the structure geometries with the given color properties. The SL models successfully captured the geometry-color relationships, while the RL algorithm bypassed the complex electromagnetic principles and time-consuming simulations, resulting in the direct inverse design of structural color with remarkable accuracy and efficiency.

2.2. Inverse design of dielectric ring arrays

2.2.1. Establishing datasets. Data acquisition is the key and fundamental part in the inverse design method. High-quality data that contains sufficient information on the dielectric arrays for structural color can provide a guarantee for the ML models with excellent learning performance. To establish the datasets that consisted of accurate and adequate data, we carefully selected and processed the geometry features that dominate the color properties and used the FEM simulation to obtain the accurate color properties. Here, we demonstrate our inverse design strategy of structural color using dielectric ring arrays. Dielectrics with a high refractive index are promising materials for structural color due to their low optical loss, strong Mie resonance, and compatibility with the fabrication process. We selected three geometry parameters: outer diameter D , inner diameter d , and the gap g between ring resonators, as marked in Fig. 2a, and three color properties: (x, y) coordinates in the CIE 1931 color space and reflection peak intensity I that are obtained from the FEM simulation, as key

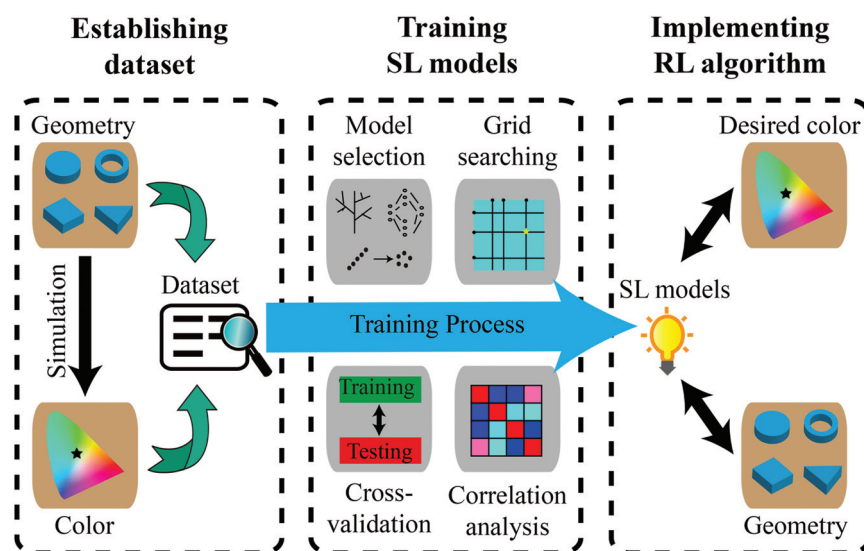


Fig. 1 Inverse design framework for structural color. The strategy consists of three key steps: establishing the datasets, training the supervised learning (SL) models, and implementing the reinforcement learning (RL) algorithm. The datasets that were made up of structure geometries and color properties were generated from simulation results. SL models were trained with input datasets to achieve high performance through the optimization techniques. The RL algorithm was implemented with the help of trained SL models to efficiently identify the structure geometries with the given color properties.

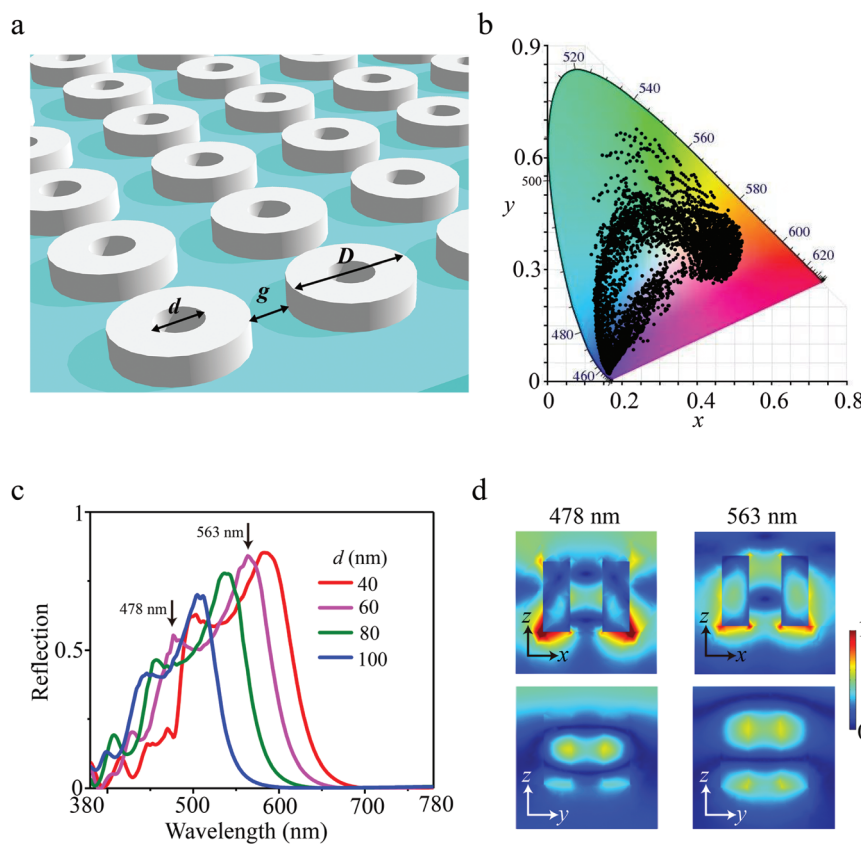


Fig. 2 Dielectric ring arrays for structural color. (a) A schematic diagram of the ring arrays. (b) The 3876 colors (solid black dots), generated by the ring arrays, are presented in CIE 1931 color space. The results were obtained using the finite element method (FEM) simulation. (c) The reflection spectra of the ring arrays where $D = 160$ nm, $g = 100$ nm, and $d = 40, 60, 80$, and 100 nm, respectively. The black arrows indicate the two selected resonances of the ring arrays when $d = 60$ nm. (d) The electric field distributions of the cross-section at the two selected resonances.

features to establish the dataset in the inverse design of the ring arrays. These features describe completely the structural color system and provide sufficient information for the training of the ML models. We simulated 3876 ring arrays and the color distribution in the CIE 1931 color space is presented in Fig. 2b. As a result, we established the dataset with six features consisting of 3876 ring arrays for the next training process. The reflection spectra of the ring arrays with $D = 160$ nm, $g = 100$ nm, and $d = 40, 60, 80$, and 100 nm, respectively, are shown in Fig. 2c. The typical peaks are attributed to the Mie resonances of the ring resonators. Fig. 2d illustrates the electric field distributions of the cross-section at the two selected resonances, which are denoted by black arrows in Fig. 2c. The Mie resonances offer a strong light matter interaction that enhances the local field distribution, and this results in the high brightness of the colors in a wide range.

2.2.2. Training of the SL models. The ML models play key roles in data analysis, behavior prediction and in guiding decisions. The well-trained SL models in the structural color system can capture the geometry-color relationships and provide reliable and accurate prediction results. In the training process, three SL models: the forward kernel ridge regression (KRR) model, the support vector classification (SVC) model, and the backward KRR model, are trained with the input

dataset. The forward KRR model is trained to predict (x, y) coordinates based on given D , d and g values. The SVC model is trained to classify the color brightness based on given D , d and g values. The backward KRR model is trained to estimate the initial geometries based on desired (x, y) coordinates (the details for the SL models are given in the Methods section). The performances of these trained SL models have been improved significantly using optimization techniques such as grid searching and cross-validation, which provide a guarantee for the successful inverse design of structural color.

To predict (x, y) based on the given D , d and g values, we employed four regression models: KRR, Gaussian process regression (GPR), decision tree regression (DTR) and multi-layer perceptron regression (MLPR), due to their abilities to handle nonlinear relationships. We randomly split the input dataset into two parts. A dataset of 800 ring arrays served as the test set and a dataset of the remaining arrays served as the training set (the learning performance of the KRR model with a different training ratio is given in ESI Fig. 1†). The four regression models were trained with the identical training set and were then applied to the identical test set. The coefficient of determination (R^2) and the training-test time (T) were used as evaluation standards to evaluate the performance of each regression model. The training-test time is the amount of time

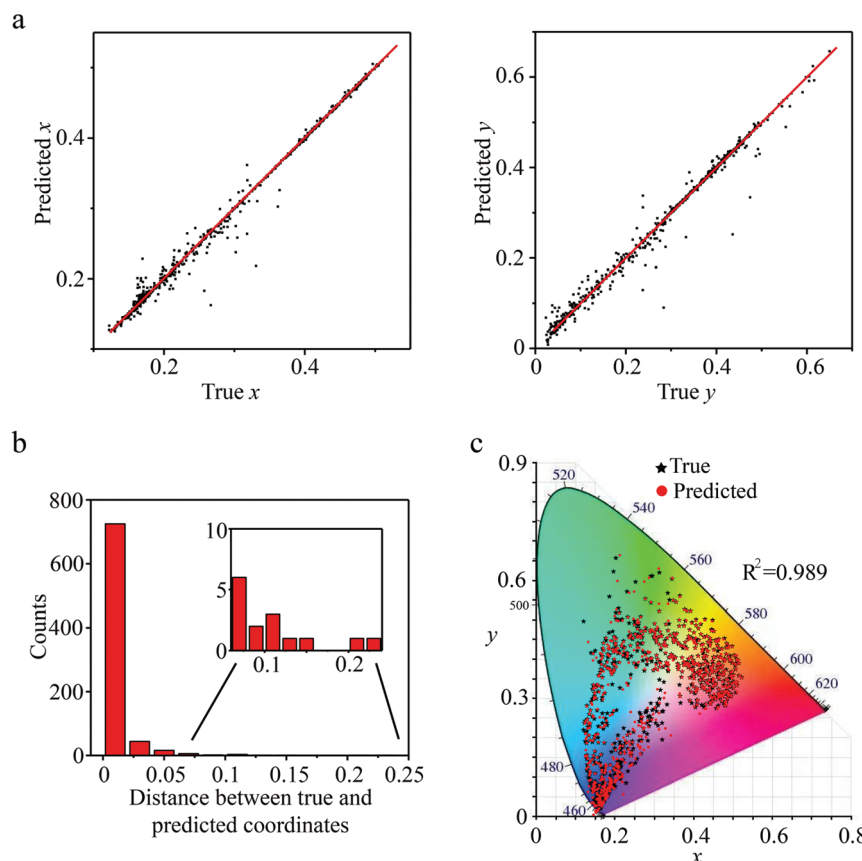


Fig. 3 Learning performance of the forward kernel ridge regression (KRR) model for color prediction on a test set that consists of 800 ring arrays. (a) Scatter plots of the true coordinates (x, y) and the predicted coordinates (x, y) in the CIE 1931 color space. (b) The counts of regular residual of the forward KRR model according to the distance between the true coordinates and the predicted coordinates. (c) The true colors (solid black stars) and the predicted colors (solid red dots) in CIE 1931 color space. The coefficient of determination (R^2) is calculated in order to estimate the prediction accuracy.

the regression models spend to be trained with the training set and then obtain the predicted colors using the test set. The DTR model finds it difficult to handle complex nonlinear relationships. The GPR and MLPR models suffer from time-consuming training processes. The KRR model is good at dealing with nonlinear relationships and has a simple training process, which makes it best suitable for color prediction. Among the four employed regression models, the KRR model is less time-consuming and reproduces the best agreement to the true coordinates. R^2 and T for the KRR model are 0.989 and 1.6 seconds, respectively. The outstanding performance of the KRR model is attributed to the kernel function that is well suited in predicting the color properties of the dielectric arrays and the low algorithm complexity of the KRR model. Fig. 3 presents the test results of the KRR model. The scatter plots of the true (x, y) coordinates and the predicted (x, y) coordinates are illustrated in Fig. 3a, indicating great consistency between the true and the predicted coordinates. The counts of regular residual according to the distance between the true coordinates and the predicted coordinates are depicted in Fig. 3b, showing obvious convergence behaviors (the performances of the other three regression models are given in ESI Table 1 and

ESI Fig. 2 and 3†). We plotted the true colors (solid black stars) and the predicted colors (solid red dots) in the CIE 1931 color space, as shown in Fig. 3c. The predicted colors are located very close to the corresponding true colors. Compared to a few days required by the FEM simulation, the computing time using the pre-trained KRR model can be dramatically decreased to a few seconds to predict the color properties from thousands of geometries with high accuracy (Intel(R) Core(TM) i5-4590 CPU), and this provides a useful tool in the inverse design of structural color. We denoted the trained KRR model as the forward KRR model and applied the forward KRR model in the optimization process of the RL algorithm, which will be discussed in the inverse design process.

To further uncover the relationship between the geometries and color properties, the heat map of the Pearson correlation coefficient matrix is presented in Fig. 4a. The positive values of the correlation coefficient indicate positive correlations, while the negative values indicate negative correlations between pairs of features. The larger the absolute value is, the bigger the relevance between features is. The correlation coefficients between D and the color properties x, y and I is 0.54, 0.43 and 0.48, respectively, which are significantly larger than the coeffi-

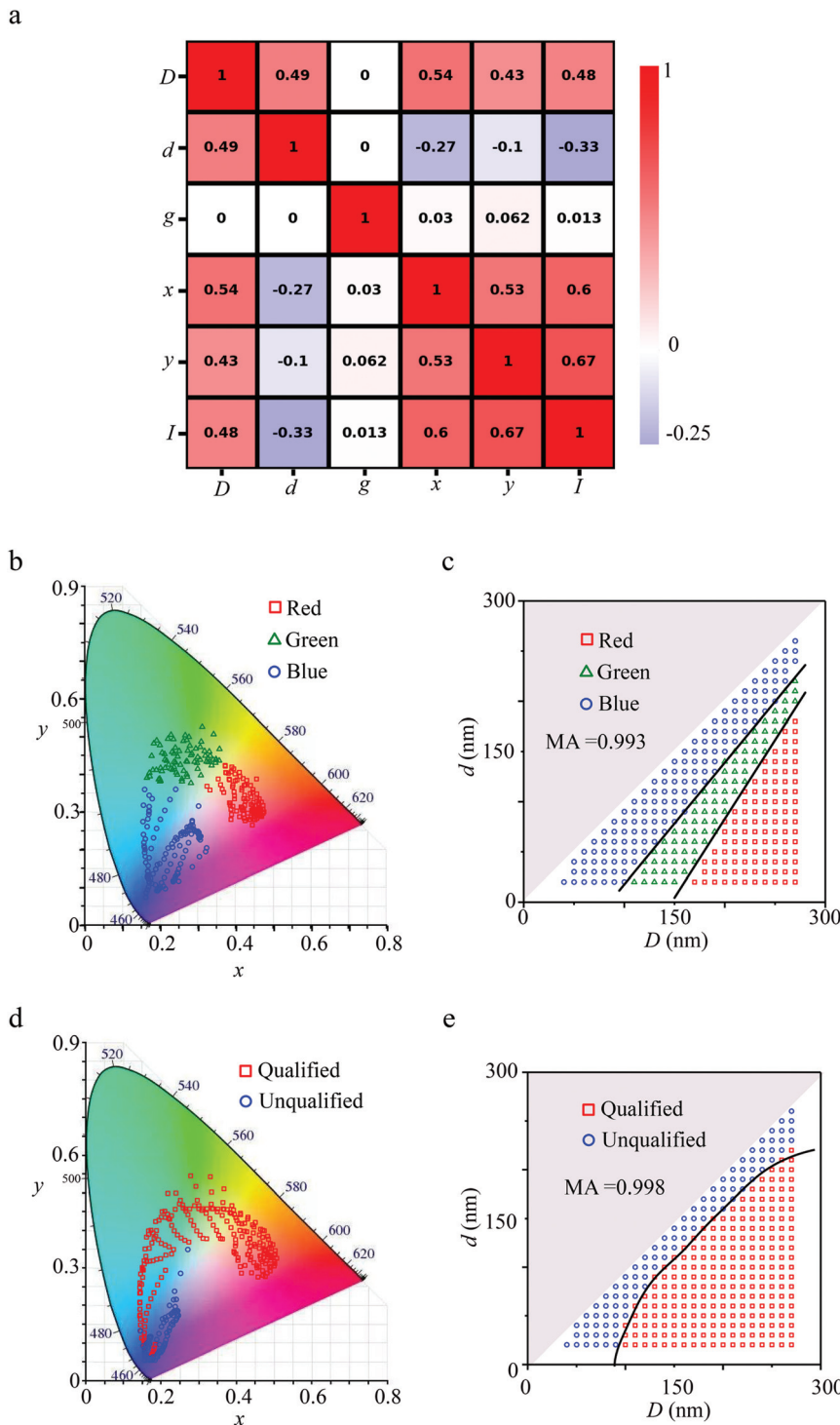


Fig. 4 Correlation analysis and support vector classification (SVC) results. (a) The heat map of the Pearson correlation coefficient matrix within six features of the ring array (outer diameter D , inner diameter d , gap g between ring resonators, (x, y) coordinates in CIE color space, and the reflection peak intensity I). (b) The colors generated by 323 ring arrays with different D and d values, and fixed $g = 20$ nm, are divided into three color categories (red, green, and blue) according to (x, y) and are presented in the CIE 1931 color space. (c) SVC results of the three color categories (red, green, and blue) in the D - d plane. The black lines indicate the linear separating hyperplanes. The mean accuracy (MA) was calculated to evaluate the classification result. (d) The colors generated by 323 ring arrays with different D and d values, and fixed $g = 40$ nm, are divided into two color categories (qualified and unqualified), according to I and are presented in the CIE 1931 color space. (e) SVC results of the two color categories (qualified and unqualified) in the D - d plane. The black curve indicates the nonlinear separating hyperplane. The mean accuracy (MA) was calculated to evaluate the classification results.

cient values between d and the color properties of -0.27 , -0.1 and -0.33 . It turns out that D plays the most significant role in determining the color properties, and d also plays a part. In addition, the correlation coefficient between g and the color properties x , y and I is one order of magnitude smaller than that between D and the color properties, and this shows that g hardly affects the color properties. It can be explained that optical resonances in high-index dielectric resonators mainly rely on the geometries of a single resonator rather than coupling between adjacent resonators, due to the field confinement within a single resonator. The datasets are grouped by g values to obtain 12 groups that consist of 323 ring arrays with the same g value. We labelled the ring arrays according to their corresponding color properties and trained the SVC models to classify the geometries in each dataset.

We divided the colors into three categories: red, green and blue, according to the distance between the (x, y) coordinates of the ring arrays and the coordinates of the standard Red Green Blue (sRBG) in the CIE 1931 color space, as presented in Fig. 4b. We trained the SVC model with linear kernel using the input dataset consisting of 323 ring arrays where $g = 20$ nm (the details of other g groups are given in ESI Fig. 4†). We classified the geometries into three categories and drew optimal separating hyperplanes (black lines), as depicted in Fig. 4c. The mean accuracy (MA) of the classification results for the total dataset was 0.939 (MA of other g groups are given in ESI Table 2†). The direction of the separating hyperplanes indicates that ring arrays with a large D value and a small d value tend to produce red colors, while ring arrays with a small D value and a large d value tend to produce blue colors. Geometries of ring arrays that generate a green color lie between the red group and the blue group. It can be explained that an increase in the length of the ring resonator in the polarization direction will decrease the frequency of the Mie resonances, resulting in a redshift in the reflection peak.

In addition to the frequency of the reflection peaks, peak intensity is another key factor in determining the color quality. Dielectric arrays that suffer from low reflectivity are inefficient and energy consuming for structural color. It is necessary to select the qualified colors with high brightness to achieve industry standard. We selected $I = 60\%$ as a threshold to distinguish between the qualified and the unqualified colors and to label ring arrays with peak intensities above and below 60%, respectively. Fig. 4d depicts qualified and unqualified colors in the CIE 1931 color space, showing that ring arrays can produce high brightness colors in a wide range. We trained the SVC model with a radial basis function (RBF) kernel using the input dataset consisting of 323 ring arrays where $g = 40$ nm (the details of other g groups are given in ESI Fig. 5†). We classified the geometries into qualified and unqualified categories and drew a nonlinear separating hyperplane, as depicted in Fig. 4e. The MA of the classification results for the total dataset was 0.998, thus providing reliable and rapid screening for the qualified colors (MA = 1.0 for $g = 10$ nm to 110 nm and MA = 0.993 for $g = 120$ nm). We applied the SVC

model to select the qualified colors in the optimization process of the RL algorithm.

2.2.3. The RL algorithm. Usually, it is unlikely to directly be able to obtain the geometry based on the desired color simply by training a SL model, due to the non-uniqueness of a solution. For a desired color, several geometries always exist. We solved this problem by implementing a RL algorithm. The geometry parameters are first slightly changed and the feedback is obtained according to the color variation in every RL round. If the color becomes closer to the desired color in the CIE color map, the geometry parameters will be changed in the same way in the next RL round. After several RL rounds, the geometry parameters that generate the desired color will be obtained. In the RL algorithm, the initial geometry parameters and optimization algorithm are two key factors that determine the efficiency and precision of the inverse design.

To obtain sensible initial geometry parameters, we imposed some restrictions on the geometry features. For a target color, we predefined two geometry features and predicted the remaining geometry feature. Due to the largest relevancy between D and (x, y) , we trained a KRR model, referred to as the backward KRR model, to predict D based on the desired (x, y) , and predefined d and g values. The backward KRR model was trained with the training set and was then applied to the test set. Fig. 5a presents the scatter plot of the true D values and the predicted D values. R^2 and T are 0.982 and 0.6 seconds, respectively. The counts of regular residual are depicted in Fig. 5b, showing obvious convergence behaviors. The backward KRR model can predict a relatively reasonable geometry based on the desired color, serving as the initial geometry in the optimization process of the RL algorithm. Since there are several geometry parameters to be optimized, we used the greedy algorithm to improve the optimization efficiency.

Fig. 5c illustrates the RL algorithm. In the first step, the backward KRR model was used to generate the initial geometry for the desired (x, y) coordinates. We chose predefined values of $d = 120$ nm and $g = 60$ nm. Different predefined d and g values may lead to different local optimal geometries but similar colors (the details of predefining d and g are discussed in ESI Table 3†). In the second step, the greedy algorithm was implemented to optimize each geometry feature in turn. For each geometry feature, the initial value was increased and decreased, respectively, until the distance between the predicted color and the desired color reached a minimum, and then the two minimums were compared to find the current optimal value for that optimization round. The (x, y) coordinates of the current geometry were predicted using the forward KRR model and the difference between the desired (x, y) coordinates supplied the feedback to guide us in updating the geometry. Within every update, the SVC model was employed to screen for the qualified colors. After several optimization rounds, D , d and g converged on one of the possible geometries with the desired colors. The greedy algorithm eliminated the coupling among the geometry features to

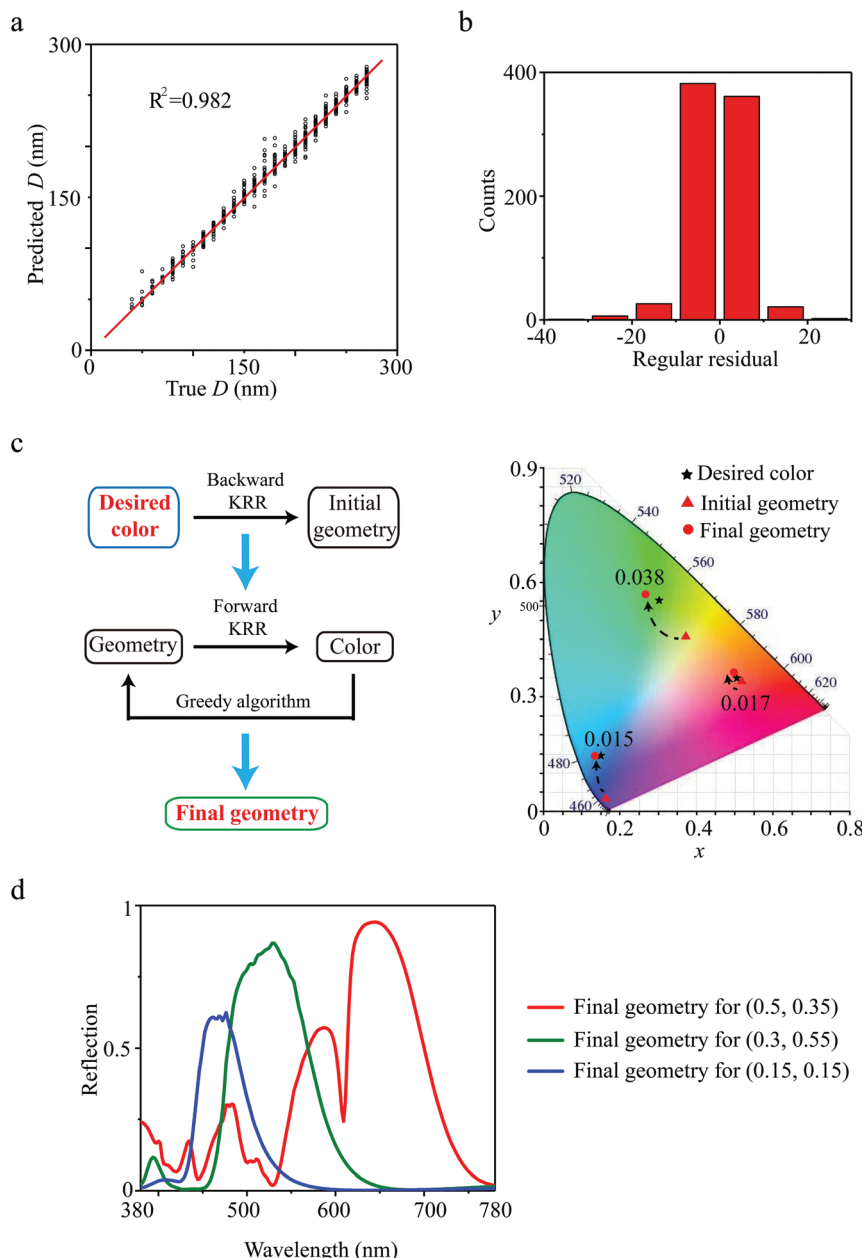


Fig. 5 The learning performance of the backward KRR model on the test, consisting of 800 ring arrays, and the reinforcement learning (RL) process. (a) The scatter plot of the true D value and the predicted D value. The coefficient of determination (R^2) was calculated to estimate the prediction accuracy. (b) The counts of regular residual of the backward KRR model. (c) The RL process. For a desired color (solid black stars), we first applied the backward KRR model to estimate initial geometries (solid red triangles), and then optimized these geometries using the greedy algorithm to obtain the final geometries (solid red circle). The forward KRR model was used to accelerate the optimization procedure, and the SVC model was used to select the qualified colors. The distances between the colors generated by the final geometries and the desired colors are presented in CIE 1931 color space. (d) FEM simulated reflection spectra of the final ring array geometries.

efficiently find the optimal solution. The accuracy of this algorithm can be guaranteed by the sensible initial geometry obtained from the backward KRR model and the sufficient restrictions imposed by the forward KRR model and SVC model. We applied the FEM simulation to verify the geometries and demonstrate the inverse design process in the CIE 1931 color space. The distances between the colors generated by the final geometries and the desired colors are shown in

the CIE 1931 color space, indicating the high precision of our inverse design strategy. Fig. 5d illustrates the FEM simulated reflection spectra of the final geometries, which show high reflection.

2.3. Inverse design of dielectric pyramid arrays

The proposed inverse design strategy is expected to be capable of the inverse design of other optical arrays, such as resonators

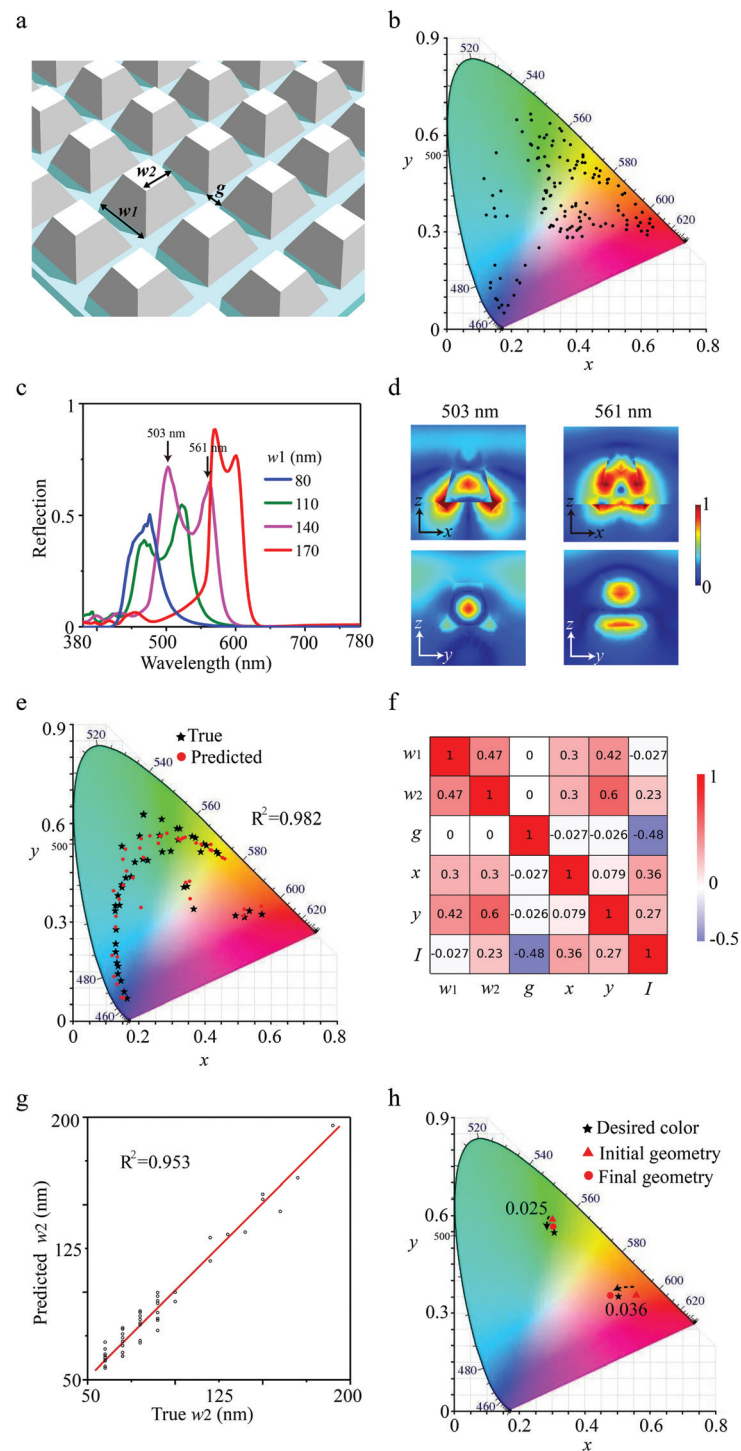


Fig. 6 The inverse design of dielectric pyramid arrays. (a) A schematic diagram of the pyramid arrays. (b) The 140 colors (solid black dots) that were generated by the pyramid arrays are presented in CIE 1931 color space. The results were obtained from FEM simulations. (c) The reflection spectra of the ring arrays, where $w_2 = 80$ nm, $g = 60$ nm, and $w_1 = 80, 110, 140$, and 170 nm, respectively. The black arrows indicate the two selected resonances of the pyramid arrays when $w_1 = 140$ nm. (d) The electric field distributions of the cross-section at the two selected resonances. (e) Learning performance of the forward KRR model for color prediction on a test set that consists of 46 pyramid arrays. The true colors (solid black stars) and the predicted colors (solid red dots) are shown in CIE 1931 color space. (f) The heat map of the Pearson correlation coefficient matrix among six features of the pyramid array (lower side length, w_1 , upper side length, w_2 , the gap, g , between pyramid resonators, the (x, y) coordinates in CIE color space, and the reflection peak intensity I). (g) The learning performance of the backward multi-layer perception regression (MLPR) model on a test set that consists of 46 pyramid arrays is presented in the scatter plot of the true w_2 and the predicted w_2 values. R^2 was calculated to estimate the prediction accuracy. (h) The inverse design process. For a desired color (solid black stars), we first applied the backward KRR model to estimate initial geometries (solid red triangles), and then optimized these geometries using the greedy algorithm to obtain the final geometries (solid red circle). The distances between the colors generated by the final geometries and the desired colors are presented in the CIE 1931 color space.

with various other more general shapes. Here, we demonstrate that our inverse design strategy of structural color is also valid in dielectric pyramid arrays. The dataset of pyramid arrays consisted of three geometry features: the lower side length, w_1 , the upper side length, w_2 , and the gap, g , between pyramid resonators, as illustrated in Fig. 6a, and three color features: (x, y) coordinates in the CIE 1931 color space and reflection peak intensity, I , which can be obtained from the FEM simulation. We simulated 140 pyramid arrays and present the color distribution in the CIE 1931 color space in Fig. 6b. As a result, we established the dataset with six features consisting of 140 pyramid arrays for the next training process. Fig. 6c and d demonstrate the optical response of the pyramid arrays. Two resonance peaks can be attributed to the electric and magnetic dipolar resonances. The dipole resonances offer strong enhancement of the near field to achieve high reflectivity and wide range tunability. The forward KRR model that is used to predict the (x, y) coordinates based on w_1 , w_2 and g exhibits a high performance of R^2 of 96.1% in the test set. The true colors (solid black stars) and predicted colors (solid red dots) in the CIE 1931 color space are illustrated in Fig. 5e. Fig. 5f depicts the heat map of the Pearson correlation coefficient matrix (the details of the color categories are given in ESI Fig. 6 and 7†). It shows that, w_1 and w_2 play key roles in determining the CIE color coordinates, while w_2 and g make a difference in affecting the reflection peak intensity. The resonance frequencies rely on the geometry of the single resonators. When pyramid resonators with a dipolar Mie resonance get closer, the magnitude of resonant modes can be effectively enhanced due to the near-field interaction. Due to the largest relevancy between w_2 and (x, y) , we trained the backward MLPR model to predict w_2 based on desired (x, y) coordinates and predefined the w_1 and g values. Fig. 6g presents the scatter plot of the true w_2 values and the predicted w_2 values. The backward MLPR model can predict a relatively reasonable geometry based on the desired color with $R^2 = 0.953$. Fig. 6h illustrates the inverse design of two colors. The distances between the colors generated by the final geometries and the desired colors show the high precision of our inverse design strategy. Our inverse design strategy can achieve high precision in a short time using a small size of the input dataset for the training processes.

3. Conclusions

The ML technology has successfully enabled the inverse design of structural color. Through training the ML models, we transformed this complex physical problem into a simple computing problem. The inverse design strategy bypasses complicated electromagnetic theory in searching for geometries for the desired colors, and so greatly accelerates the design of structural color with high accuracy. Moreover, our strategy provides a new way to solve the inverse problem that usually involves non-unique solutions. Each possible solution can be considered as a local optimum that appropriately coincides

with the global optimum. An excellent initial value and efficient optimization algorithm are key factors in achieving such local optimum values, which can be properly handled using well-trained SL models. The proposed inverse design strategy is applicable to complicated physical systems with large numbers of features.

4. Methods

4.1. Regression models

The Kernel Ridge Regression (KRR) model combines ridge regression (linear least squares with l2-norm regularization) with the kernel trick. It can determine nonlinear relationships by mapping the data in the original space to new spaces with different nonlinear kernels. The Decision Tree Regression (DTR) model splits the dataset into several parts and adopts linear regression for each part. Overfitting would occur if the tree depth is too large. The Multi-Layer Perception Regression (MLPR) model consists of an input layer, hidden layers and an output layer. It can determine nonlinear functions with the nonlinear hidden layers. It is sometimes hard to achieve a global optimal solution. The key principle of Gaussian Process Regression (GPR) is using infinite dimension multivariate Gaussian distribution to model the function. Every sample in the input dataset is linked to a random variance. This model becomes extremely inefficient in highly dimensional space. All the regression models are in the open-source scikit-learn package.

4.2. Classification model

The key principle of the support vector classification (SVC) model is to find the optimal classification hyperplane, which makes the largest distances between the different classes. The Lagrangian optimization method and Kuhn-Tucker (KKT) conditions are involved in SVC model training. SVC can solve the linear inseparable problem with a nonlinear kernel. The SVC model is in the open-source scikit-learn package.

4.3. Reinforcement learning

Through interaction with environments, AI obtains feedback to help guide its behaviors. In the optimization step, the difference between the predicted and the given colors serves as feedback.

4.4. Greedy algorithm

The key principle of the greedy algorithm in solving the problem is to find the local optimal solution that neglects the global condition. The greedy algorithm is an efficient optimization method because it ignores the complicated coupling between different parameters.

4.5. Hyper-parameter selection and cross-validation

Hyper-parameters were predefined parameters of the ML models, and these determined the performance of the ML models in given problems. A set of optimal hyper-parameters

was crucial for improving the efficiency and generalization performance. Cross-validation is a statistical method that splits the training dataset into several parts for training and testing, respectively, in order to improve the generalization performance of the ML models. It is often used in the selection process of hyper-parameters to verify the performance of the model.

4.6. Numerical simulations

Numerical simulations were performed using COMSOL Multiphysics, a finite-element analysis and solver software. The simulations were implemented in the 3D radio frequency (RF) module, including the actual geometric size and relevant properties. The system consisted of the Si resonators on the SiO_2 substrate surrounded by air. The optical properties for Si were taken from the Handbook of Optical Constants of Solids. The thickness of the resonators was fixed at 130 nm. For calculating the reflection spectra, a p-polarized plane wave was launched within the x - z plane at a normal incidence in the visible range.

Author contributions

J. Z. conceived the project. Z. H. carried out ML predictions. Z. H. and X. L. carried out the FEM calculations. Z. H. and J. Z. wrote the paper, with all authors contributing to the discussion and preparation of the manuscript.

Conflicts of interest

The authors declare no competing interests.

Acknowledgements

This work was supported by the National Key Research and Development Program of China (2018YFB1105100), the National Natural Science Foundation of China (51572096 and 51820105008), and the Innovation Fund of WNLO.

References

- 1 N. I. Zheludev and Y. S. Kivshar, From metamaterials to metadevices, *Nat. Mater.*, 2012, **11**(11), 917–924.
- 2 D. Marpaung, J. Yao and J. Capmany, Integrated microwave photonics, *Nat. Photonics*, 2019, **13**(2), 80–90.
- 3 I. Stavrinou and J. Schilling, Metamaterial-inspired silicon nanophotonics, *Nat. Photonics*, 2017, **11**(5), 274–284.
- 4 Y. Li, S. Kita, P. Muñoz, O. Reshef, D. I. Vulis, M. Yin, M. Lončar and E. Mazur, On-chip zero-index metamaterials, *Nat. Photonics*, 2015, **9**(11), 738–742.
- 5 Y. Yang, Z. Gao, H. Xue, L. Zhang, M. He, Z. Yang, R. Singh, Y. Chong, B. Zhang and H. Chen, Realization of a three-dimensional photonic topological insulator, *Nature*, 2019, **565**(7741), 622–626.
- 6 S. Molesky, Z. Lin, A. Y. Piggott, W. Jin, J. Vucković and A. W. Rodriguez, Inverse design in nanophotonics, *Nat. Photonics*, 2018, **12**(11), 659–670.
- 7 J. Riishede and O. Sigmund, Inverse design of dispersion compensating optical fiber using topology optimization, *J. Opt. Soc. Am. B*, 2008, **25**(1), 88–97.
- 8 S. Preble, M. Lipson and H. Lipson, Two-dimensional photonic crystals designed by evolutionary algorithms, *Appl. Phys. Lett.*, 2005, **86**(6), 061111.
- 9 M. I. Jordan and T. M. Mitchell, Machine learning: Trends, perspectives, and prospects, *Science*, 2015, **349**(6245), 255–260.
- 10 Z. Ghahramani, Probabilistic machine learning and artificial intelligence, *Nature*, 2015, **521**(7553), 452–459.
- 11 G. Carleo and M. Troyer, Solving the quantum many-body problem with artificial neural networks, *Science*, 2017, **355**(6325), 602–606.
- 12 H. K. Lau, R. Pooser, G. Siopsis and C. Weedbrook, Quantum Machine Learning over Infinite Dimensions, *Phys. Rev. Lett.*, 2017, **118**(8), 080501.
- 13 D.-L. Deng, X. Li and S. Das Sarma, Machine learning topological states, *Phys. Rev. B*, 2017, **96**(19), 195145.
- 14 K. T. Butler, D. W. Davies, H. Cartwright, O. Isayev and A. Walsh, Machine learning for molecular and materials science, *Nature*, 2018, **559**(7715), 547–555.
- 15 B. Sanchez-Lengeling and A. Aspuru-Guzik, Inverse molecular design using machine learning: Generative models for matter engineering, *Science*, 2018, **361**(6400), 360–365.
- 16 M. Reichstein, G. Camps-Valls, B. Stevens, M. Jung, J. Denzler and N. Carvalhais, Prabhat, Deep learning and process understanding for data-driven Earth system science, *Nature*, 2019, **566**(7743), 195–204.
- 17 A. Radovic, M. Williams, D. Rousseau, M. Kagan, D. Bonacorsi, A. Himmel, A. Aurisano, K. Terao and T. Wongjirad, Machine learning at the energy and intensity frontiers of particle physics, *Nature*, 2018, **560**(7716), 41–48.
- 18 M. Popova, O. Isayev and A. Tropsha, Deep reinforcement learning for de novo drug design, *Sci. Adv.*, 2018, **4**(7), 7885.
- 19 Y. Dong, C. Wu, C. Zhang, Y. Liu, J. Cheng and J. Lin, Deep Learning Bandgaps of Topologically Doped Graphene, *arXiv:1809.10860*, 2018.
- 20 S. Lu, Q. Zhou, Y. Ouyang, Y. Guo, Q. Li and J. Wang, Accelerated discovery of stable lead-free hybrid organic-inorganic perovskites via machine learning, *Nat. Commun.*, 2018, **9**(1), 3405.
- 21 S. P. Collins, T. D. Daff, S. S. Piotrkowski and T. K. Woo, Materials design by evolutionary optimization of functional groups in metal-organic frameworks, *Sci. Adv.*, 2016, **2**(11), 1600954.
- 22 M. W. Libbrecht and W. S. Noble, Machine learning applications in genetics and genomics, *Nat. Rev. Genet.*, 2015, **16**(6), 321–332.

- 23 M. Wainberg, D. Merico, A. Delong and B. J. Frey, Deep learning in biomedicine, *Nat. Biotechnol.*, 2018, **36**(9), 829–838.
- 24 M. Narhi, L. Salmela, J. Toivonen, C. Billet, J. M. Dudley and G. Genty, Machine learning analysis of extreme events in optical fibre modulation instability, *Nat. Commun.*, 2018, **9**(1), 4923.
- 25 S. S. Kalantre, J. P. Zwolak, S. Ragole, X. Wu, N. M. Zimmerman, M. D. Stewart and J. M. Taylor, Machine learning techniques for state recognition and auto-tuning in quantum dots, *Npj Quantum Inf.*, 2019, **5**, 1.
- 26 D. Zibar, M. Piels, R. Jones and C. G. Schaeffer, Machine Learning Techniques in Optical Communication, *J. Lightwave Technol.*, 2016, **34**(6), 1442–1452.
- 27 P. Zhang, H. Shen and H. Zhai, Machine Learning Topological Invariants with Neural Networks, *Phys. Rev. Lett.*, 2018, **120**(6), 066401.
- 28 M. Turduev, E. Bor, C. Latifoglu, I. H. Giden, Y. S. Hanay and H. Kurt, Ultracompact Photonic Structure Design for Strong Light Confinement and Coupling Into Nanowaveguide, *J. Lightwave Technol.*, 2018, **36**(14), 2812–2819.
- 29 J. Peurifoy, Y. Shen, L. Jing, Y. Yang, F. Cano-Renteria, B. G. DeLacy, J. D. Joannopoulos, M. Tegmark and M. Soljačić, Nanophotonic particle simulation and inverse design using artificial neural networks, *arXiv:1712.03222*, 2017.
- 30 D. Liu, Y. Tan, E. Khoram and Z. Yu, Training Deep Neural Networks for the Inverse Design of Nanophotonic Structures, *ACS Photonics*, 2018, **5**(4), 1365–1369.
- 31 Y. Long, J. Ren, Y. Li and H. Chen, Inverse design of photonic topological state via machine learning, *Appl. Phys. Lett.*, 2019, **114**, 18.
- 32 S. So, J. Mun and J. Rho, Simultaneous inverse-design of material and structure via deep-learning: Demonstration of dipole resonance engineering using core-shell nanoparticles, *arXiv:1904.02848v1*, 2019.
- 33 I. Malkiel, M. Mrejen, A. Nagler, U. Arieli, L. Wolf and H. Suchowski, Plasmonic nanostructure design and characterization via Deep Learning, *Light: Sci. Appl.*, 2018, **7**(1), 60.
- 34 Y. Nagasaki, M. Suzuki and J. Takahara, All-Dielectric Dual-Color Pixel with Subwavelength Resolution, *Nano Lett.*, 2017, **17**(12), 7500–7506.
- 35 S. Sun, Z. Zhou, C. Zhang, Y. Gao, Z. Duan, S. Xiao and Q. Song, All-Dielectric Full-Color Printing with TiO₂ Metasurfaces, *ACS Nano*, 2017, **11**(5), 4445–4452.
- 36 A. E. Goodling, S. Nagelberg, B. Kaehr, C. H. Meredith, S. I. Cheon, A. P. Saunders, M. Kolle and L. D. Zarzar, Colouration by total internal reflection and interference at microscale concave interfaces, *Nature*, 2019, **566**(7745), 523–527.
- 37 Y. Nagasaki, M. Suzuki, I. Hotta and J. Takahara, Control of Si-Based All-Dielectric Printing Color through Oxidation, *ACS Photonics*, 2018, **5**(4), 1460–1466.
- 38 Y. Chen, X. Duan, M. Matuschek, Y. Zhou, F. Neubrech, H. Duan and N. Liu, Dynamic Color Displays Using Stepwise Cavity Resonators, *Nano Lett.*, 2017, **17**(9), 5555–5560.
- 39 K. T. P. Lim, H. Liu, Y. Liu and J. K. W. Yang, Holographic colour prints for enhanced optical security by combined phase and amplitude control, *Nat. Commun.*, 2019, **10**(1), 25.
- 40 J. Xue, Z.-K. Zhou, Z. Wei, R. Su, J. Lai, J. Li, C. Li, T. Zhang and X.-H. Wang, Scalable, full-colour and controllable chiralotropic plasmonic printing, *Nat. Commun.*, 2015, **6**, 8906.
- 41 V. Flauraud, M. Reyes, R. Paniagua-Domínguez, A. I. Kuznetsov and J. Brugger, Silicon Nanostructures for Bright Field Full Color Prints, *ACS Photonics*, 2017, **4**(8), 1913–1919.
- 42 Y. Zhang, Q. Zhang, X. Ouyang, D. Y. Lei, A. P. Zhang and H. Y. Tam, Ultrafast Light-Controlled Growth of Silver Nanoparticles for Direct Plasmonic Color Printing, *ACS Nano*, 2018, **12**(10), 9913–9921.
- 43 Y. Nagasaki, I. Hotta, M. Suzuki and J. Takahara, Metal-Masked Mie-Resonant Full-Color Printing for Achieving Free-Space Resolution Limit, *ACS Photonics*, 2018, **5**(9), 3849–3855.
- 44 J. S. Clausen, E. Hojlund-Nielsen, A. B. Christiansen, S. Yazdi, M. Grajower, H. Taha, U. Levy, A. Kristensen and N. A. Mortensen, Plasmonic metasurfaces for coloration of plastic consumer products, *Nano Lett.*, 2014, **14**(8), 4499–4504.
- 45 Z. Dong, J. Ho, Y. F. Yu, Y. H. Fu, R. Paniagua-Dominguez, S. Wang, A. I. Kuznetsov and J. K. W. Yang, Printing Beyond sRGB Color Gamut by Mimicking Silicon Nanostructures in Free-Space, *Nano Lett.*, 2017, **17**(12), 7620–7628.
- 46 A. S. Roberts, A. Pors, O. Albrektsen and S. I. Bozhevolnyi, Subwavelength plasmonic color printing protected for ambient use, *Nano Lett.*, 2014, **14**(2), 783–787.